Exp Fluids (2007) 43:437–451
DOI 10.1007/s00348-007-0306-2

RESEARCH ARTICLE

Viscous flow through microfabricated hyperbolic contractions

**Mónica S. Neves Oliveira · Manuel A. Alves ·
Fernando T. Pinho · Gareth H. McKinley**

Received: 10 October 2006 / Revised: 20 March 2007 / Accepted: 30 March 2007 / Published online: 17 May 2007
© Springer-Verlag 2007

Abstract We study the flow of a Newtonian fluid through microfabricated hyperbolic contractions followed by a sudden expansion, with the aim of investigating the potential of this geometry to serve as an extensional microrheometer. A set of planar converging geometries, with total Hencky strains ranging from 1.0 to 3.7, were fabricated in order to produce a homogeneous extensional flow field within the contraction. The velocity field in various planes of the hyperbolic contraction was quantified by means of microparticle image velocimetry (μPIV) and the pressure drop across the converging geometry was also measured and found to vary approximately linearly with the flow rate. Additionally, an extensive range of numerical calculations were carried out using a finite-volume method to help assess the performance of this geometry as a microfluidic elongational rheometer. The measured velocity fields in the contraction and associated pressure drops compare very well (to within 10%) with the numerical predictions. For the typical dimensions used in the microfluidic devices, the steady viscous flow through the contraction is shown to be three-dimensional and it is demonstrated that regions with nearly constant strain rate can only be achieved using geometries with large total Hencky strains under Hele–Shaw (potential-like) flow conditions.

1 Introduction

Extensionally dominated flows are particularly important in many applications involving non-Newtonian fluids, ranging from polymer processing (e.g., injection molding, spinning, and film blowing) to inkjet printing or fertilizer spraying (Barnes et al. 1989). Optimization of these processes requires accurate measurements of the extensional properties of the fluid being processed. The measurement of extensional viscosity is still a challenging task, especially when dealing with dilute polymeric solutions, since inertial effects frequently dominate the elongational stresses at high deformation rates (Hermansky and Boger 1995). One of the most promising techniques proposed for measurement of extensional viscosity involves studying the fluid flow through contractions profiled to give uniform extension rate (hyperbolic contractions) (Cogswell 1978). In this method, the pressure drop along the channel is measured to evaluate the resistance to the rate of elongational deformation, and this can then be related to an apparent extensional viscosity. To alleviate the effect of shear at the walls of contractions, Shaw (1975) proposed the use of a lubricating layer of low-viscosity fluid that is

---

M. S. N. Oliveira (✉) · M. A. Alves
Departamento de Engenharia Química, CEFT,
Faculdade de Engenharia da Universidade do Porto,
4200-465 Porto, Portugal
e-mail: monica.oliveira@fe.up.pt

M. A. Alves
e-mail: mmalves@fe.up.pt

M. S. N. Oliveira · G. H. McKinley
Department of Mechanical Engineering,
Massachusetts Institute of Technology,
Cambridge, MA 02139, USA
e-mail: gareth@mit.edu

F. T. Pinho
CEFT, Faculdade de Engenharia da Universidade do Porto,
4200-465 Porto, Portugal
e-mail: fpinho@fe.up.pt; fpinho@dem.uminho.pt

F. T. Pinho
Universidade do Minho, 4704-553 Braga, Portugal

injected at the walls near the upstream entrance. Although this is feasible for viscous fluids such as polymer melts, and results in more accurate measurements of the elongational viscosity (Everage and Ballman 1978), it is not an option when the fluids of interest are themselves low-viscosity materials (such as inks, dyes or coating fluids). In the absence of lubrication, it is thus essential to understand the perturbations to the flow that arise from the effects of shear.

James (1991) used a similarity transformation to analyze the steady flow of a Newtonian fluid in an axisymmetric converging geometry with a hyperbolic profile R^2z = constant (where $R(z)$ is the radius of the channel at the axial position z) so that the average velocity increases approximately linearly along the centerline. The analysis showed that at finite Reynolds numbers there is a homogeneous extensional flow within the central part of the contraction geometry, while the effects of shear are confined to a narrow boundary layer close to the wall. As the Reynolds number is increased further, viscous effects become less and less important, and the flow approaches a uniform potential flow in the inviscid limit. Experimental measurements and finite element calculations of the flow geometry showed good agreement with this similarity solution (James et al. 1990). Feigl et al. (2003) used the same type of converging geometry and showed that it is possible to obtain shear-free flow in which the extensional rate does not vary significantly along the core of the hyperbolic die under conditions of full slip at the walls. Although it is possible to promote wall-slip in polymer melts, it is hard to achieve complete slip in a controllable fashion, especially for low-viscosity materials.

The potential to apply similar approaches for measuring the elongational viscosity in low-viscosity fluids has been enhanced by the advent of microfluidics. The rapid development of soft lithography over the past decade has made possible the production of microfluidic devices with precise dimensions and low cost. Because of the small length-scales that characterize these flows (typically 100 μm or less), high-deformation rates are attainable in microfluidic flows, yet the Reynolds numbers remain small. A consequence of the ability to access a large range of deformation rates is that strong viscoelastic effects can be achieved in fluids that would otherwise behave essentially as Newtonian fluids in the equivalent macroscale flows (Groisman and Quake 2004; Rodd et al. 2005). Thus, microfluidics provides an excellent technology platform for the development of an extensional rheometer for dilute polymer solutions. However, there is a major difference between geometries that are attainable with microfluidic channels and the dies used by James et al. (1990) and Feigl et al. (2003): the former, fabricated using soft lithography, are typically planar, i.e., the depth is kept constant throughout the channel, while the latter are axisymmetric. Therefore, even though the general approach of James et al. (1990) was adopted to inspire the design of our microscale planar hyperbolic contractions, quantifying the level of kinematic homogeneity attained in the device is essential for attaining meaningful rheological measurements. In the present paper, we first study viscous Newtonian fluids using complementary experimental and numerical methods in order to eliminate the role of non-Newtonian effects, which further complicate the analysis.

A large number of investigations have been undertaken to understand the fundamentals of fluid flow through microfluidic devices (see for example Sharp and Adrian 2004; Stone et al. 2004; Squires and Quake 2005 and references therein). However, only a few focus on microgeometries, which involve some type of change in cross-sectional area to study extensional effects; most of these are concerned with sudden contractions or/and sudden expansions. Sudden contractions and expansion flows, which we briefly review next, are benchmark geometries for investigating the effects of viscoelasticity (Hassager 1988; Brown and Mckinley 1994). The primary benefit of focusing on microscale geometries arises from the ability to attain much higher deformation rates than those achievable at macro scales. Hence, the investigations of Rodd et al. (2005, 2007) concerned the flow of dilute and semi-dilute polymer solutions through sudden microcontractions and microexpansions using streakline photography, microparticle image velocimetry (μPIV) measurements and pressure drop measurements. Such measurements are aimed at understanding the interplay of fluid inertia and viscoelasticity and at mapping the flow transitions in a stability map controlled by the dimensionless Reynolds number and Weissenberg number, which parameterize the importance of fluid inertia and elasticity, respectively. Kang et al. (2005, 2006) also studied the pressure-driven flow of aqueous polymer solutions through microfabricated contractions and were able to achieve shear rates of up to 10^6 s^{-1}. Measurements of the pressure drop through the contractions demonstrate that there can be substantial extra pressure losses associated with the extensional flow that arises when entering or exiting the contraction region, thus hinting at a possible use as a rheometric device. However, in neither of these earlier studies were the local kinematics or dynamic pressure drops compared with corresponding numerical simulations. Tsai et al. (2006) have examined numerically the flow of Newtonian fluids through microfabricated planar expansions and demonstrated that even though the microfluidic device may have a planar geometry, the flow becomes locally 3D near the expansion region. Indeed, even for a slowly varying planar geometry, the velocity field in a microfluidic device can become highly 3D in character as demonstrated analytically by Lauga et al. (2004). Understanding and taking account of this effect is therefore important when devising rheometrical devices, especially if they contain abrupt changes in cross-section. In designing and optimizing a microfluidic geometry it is essential to combine experimental measurements possessing high spatial and temporal resolution with numerical computations of the corresponding flow field to systematically explore the sensitivity of the kinematics to changes in the geometry and the flow conditions.

This paper is organized as follows. Section 2 describes the experimental methods of device fabrication as well as the measurement techniques used for pressure drop and velocity measurements. An evaluation of the uncertainties associated with the velocity measurement technique is also undertaken, with emphasis on the effect of Brownian motion. Section 3 presents the governing equations and outlines the numerical method used in the computational investigation. In Sect. 4, we present the experimental and numerical results: we start by validating the experimental technique used for velocity measurement and then analyze in detail the effects of inertia and variations in the total Hencky strain on the extensional character of the velocity field in the contraction region. Finally, we make quantitative comparisons of experimental measurements and numerical calculations for the total pressure drop across the microfluidic rheometric device. In order to reduce the overall pressure drop across the microfluidic device, the hyperbolic contraction region is followed by a sudden expansion, and we also analyze the separated flow that develops within the expansion region. We close the paper in Sect. 5 with some general conclusions that can be used to help optimize the future design of microfluidic extensional devices.

2 Experimental methods

2.1 Channel geometry and fabrication

The microgeometries used in this work are planar in character and are designed to have a hyperbolic contraction section followed by an abrupt expansion. In theory, the converging region leads to a uniform strain rate deformation. Figure 1 shows a scanning electron microscopy (SEM) image and a white light transmission microscopy image of typical contraction-expansion geometries used in the present study. The channel depth, h, and the width of the upstream and downstream channels, $w_u = w_d$, were kept constant for all geometries used: $h = 46$ (±1) μm and $w_u = w_d = 400$ μm, respectively. The total Hencky strain experienced by a fluid element can be defined as $\varepsilon_H = \ln(w_u/w_c)$ and was varied from 1.0 to 3.7. These values correspond to the minimum contraction widths, w_c, at the expansion plane and contraction lengths, L_c, specified in Table 1. The Cartesian coordinate system used in describing our measurements is centered on the centerline, at the entrance plane of the contraction (cf. Fig. 1b). For $0 \leq z \leq L_c$, the contraction wall is shaped according to the following function: $x = C/(a+z)$, where $a = L_c w_c/(w_u - w_c) = 20$ μm and $C = L_c w_u w_c/[2(w_u - w_c)] = 4{,}000$ μm^2.

The channels were fabricated in polydimethylsiloxane (PDMS) from an SU-8 photoresist mold using standard soft-lithography techniques (McDonald et al. 2000; Ng et al. 2002). A high-resolution chrome mask together with a contrast enhancer and a barrier coat were employed to attain nearly vertical side-walls (with wall angles 87°< α < 92°) and well-defined corner features. A detailed description of the protocols for channel fabrication can be found in Scott (2004) and Rodd (2006). Pressure taps were located 3×10^{-3} m upstream and downstream of the contraction plane, which is located at $z = 0$. A constant displacement-rate syringe pump (Harvard Apparatus PHD2000) was used to impose the flow rate, Q, of fluid supplied to the microdevice ($0.4 \leq Q \leq 10$ ml/h). For our μPIV measurements, the flow rate range was narrowed to $Q \leq 3$ ml/h due to equipment limitations (i.e., the combination of channel size, objective magnification and minimum achievable time interval between two consecutive laser pulses).

2.2 Experimental methods and procedures

The results presented here were obtained using deionized water as the working fluid. The viscosity of the fluid is $\mu = 0.94 \times 10^{-3}$ Pa s and the density is $\rho = 998$ kg/m^3,

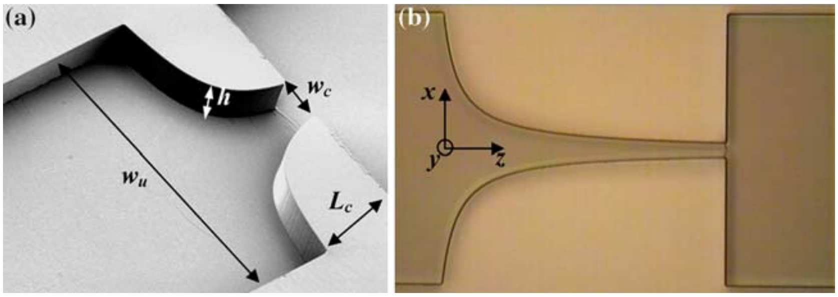

Fig. 1 Microfluidic geometry with a hyperbolic contraction for generating planar elongational flow. **a** SEM image ($\varepsilon_H = 2.0$); **b** Optical transmission microscope image ($\varepsilon_H = 3.0$)

Table 1 Geometry characteristic dimensions

Hencky strain, ε_H	L_c (μm)	w_c (μm)	h (μm)
1.0	34.4	147	46.0
2.0	128	54.1	46.0
3.0	382	19.9	46.0
3.7	780	10.0	46.0

both measured at 296 K, the average temperature at which the experiments were carried out.

The flow through the contraction region was characterized experimentally using μPIV in conjunction with measurements of the total pressure drop across the contraction region. The pressure drop measurements associated with viscous flow through the microfluidic device were measured using a calibrated differential pressure sensor (Honeywell 26PC), with a maximum measurable differential pressure of 3.5×10^4 Pa, connected via flexible tubing to the two pressure taps.

The μPIV technique was developed to quantify the hydrodynamics inside microfluidic devices (Santiago et al. 1998). This technique incorporates many of the basic principles of PIV for measuring local velocity components from the average displacement of tracer particles (Δx) in an interrogation region over a known time (Δt) (Wereley and Meinhart 2004). This process is carried out using a double-frame imaging technique with a cross-correlation algorithm for extracting local particle displacements. There are two main differences between μPIV and traditional PIV: first, in μPIV a microscope lens must be coupled to the digital imaging camera used in standard PIV; second, whereas the thickness of the light-sheet dictates the out-of-plane resolution in standard PIV, μPIV relies on volume illumination and, consequently, the thickness of the measurement domain is defined by the numerical aperture and magnification of the high-resolution optical system used (Meinhart et al. 2000).

In the present work, a CCD camera (PCO SensicamQE; 1376 × 1024 pixels) connected to an inverted microscope (Nikon TE2000-S) with a 20X objective lens (numerical aperture, NA = 0.5) was used to acquire the images in specific z–x planes. For volume-illumination of the flow, we used a double-pulsed Solo Nd:YAG laser system (15×10^{-3} J/pulse; New Wave Research, Fremont, CA) with a wavelength of $\lambda = 532$ nm. As tracer particles, we employed 0.5 μm diameter red fluorescent particles (Molecular Probes, Eugene, OR, USA, Ex/Em = 520/580 nm). The time separation between two consecutive frames was adjusted over the range of 2.1–100 μs, depending on flow conditions and the region of the contraction geometry under focus in order to satisfy the constraint $2d_p < \Delta x < 7.5d_p$ (Rodd 2006). For all cases, a minimum of 70 image pairs were recorded, divided into interrogation areas of 32 × 32 pixels. These images were processed and ensemble averaged using the Insight software package from TSI (Version 6.1.1.0). For processing, we used a Nyquist algorithm with a 50% overlap to generate the 2D velocity vector maps.

The resolution and accuracy of the μPIV measurements are affected by a number of factors, which include issues such as spatial and temporal resolution, particle visibility and Brownian fluctuations of the tracer particles (Wereley and Meinhart 2004).

2.2.1 *Spatial resolution*

The effective particle image size is crucial in terms of the uncertainty in the location of correlation peak from which the velocity measurements are calculated. This effective size projected back into the flow, d_e/M, is calculated as the convolution of the diffraction-limited spot size of a point source of light, d_s, with the geometric image (Wereley and Meinhart 2004):

$$d_s = 2.44(M+1)\frac{\lambda}{2(\mathrm{NA})}, \tag{1}$$

$$d_e = \left(d_s^2 + M^2 d_p^2\right)^{1/2}, \tag{2}$$

where d_p is the true particle diameter, M the magnification, NA the numerical aperture of the objective and λ is the wavelength of the imaged light. Provided the particle image takes up 3–4 pixels, the uncertainty in the correlation peak can be calculated as $d_e/(10M)$ (Prasad et al. 1992). For our optical set-up, this amounts to 0.16 μm. The in-plane spatial resolution of the velocity vectors is defined by the size of the interrogation area used to determine a single velocity vector, i.e., 32 × 32 pixels in our case.

For an optical system, to define the out-of-plane spatial resolution it is typical to calculate the depth of field as:

$$\delta z = \frac{n\lambda}{(\mathrm{NA})^2} + \frac{ne}{(\mathrm{NA})\,M} \tag{3}$$

provided that $d_p > e/M$, where e is the minimum resolvable feature size, and n is the refractive index of the medium. For our specific optical set-up, $e/M = 0.32$ μm is smaller than the diameter of the tracer particles (0.5 μm) and the depth of field can be evaluated using Eq. 3, leading to $\delta z = 0.86$ μm. However, this value is misrepresentative of the true thickness of the measurement domain over which particle information contributes to the correlation peak. According to Meinhart et al. (2000), the true depth of measurement (δz_m) can be calculated as a sum of three components associated with diffraction, geometrical shadow and particle size:

$$\delta z_{\mathrm{m}} = \frac{3n\lambda}{\mathrm{NA}^2} + \frac{2.16 d_{\mathrm{p}}}{\tan\theta} + d_{\mathrm{p}}, \tag{4}$$

where θ is the collection angle of the optical system, $\theta = \sin^{-1}$ (NA/n). The calculated depth of measurement for our optical system is 11.7 μm, which amounts to 25% of the channel depth.

2.2.2 *Particle visibility*

An important consequence of volume-illumination is that all particles in the illuminated volume will contribute to the recorded image (Wereley et al. 2002). Thus, light from unfocused particles will contribute to the background intensity level, which may hinder in-focus particle visibility. Olsen and Adrian (2000) have considered this issue in detail and define particle visibility (Vis) as the ratio of the peak intensity of an in-focus particle to the background intensity. They found that the visibility of a particle is dependent on the numerical aperture of the optical set-up and only weakly dependent on magnification. Furthermore, for a specific optical set-up, particle visibility is a function of particle size, channel depth and inversely proportional to particle concentration as described in Eq. 14 of Olsen and Adrian (2000). Following these authors, it is necessary that the particle concentration does not exceed 0.11% by volume for our specific case in order to obtain a minimum particle visibility of Vis = 1.5 (Rodd 2006). This critical concentration is substantially higher than the actual particle concentration used (0.02% by volume) and to overcome the corresponding low-density images, an ensemble averaging technique was used. This has the advantages of increasing the signal-to-noise ratios in the correlation function, increasing the success rate for resolving a correlation peak for each interrogation area and decreasing the error in the measured velocity.

2.2.3 *Brownian motion*

For reliable measurements, tracer particles should follow exactly the fluid flow without interfering with the bulk fluid velocity. In microfluidics, when tracer particles have submicron sizes and the characteristic velocity is small, Brownian motion can, to some degree, inhibit the particles from following the flow and introduce an error in the measurement (Wereley et al. 2002). Santiago et al. (1998) estimated the error due to Brownian motion relative to the total particle displacement as:

$$\epsilon_{\mathrm{B}} = \frac{\sigma}{\delta} = \frac{1}{V}\sqrt{\frac{2D}{\delta t}}, \tag{5}$$

where D is the diffusion coefficient for the spherical tracer particles, $D = k_{\mathrm{B}}T/(3\pi\ \mu\ d_{\mathrm{p}})$ (Einstein 1905), σ the displacement due to Brownian motion, δ the total particle displacement, δt the time interval between images, V the characteristic velocity, k_{B} the Boltzmann's constant, T the absolute temperature of the fluid and μ is the dynamic viscosity. The largest error due to Brownian motion will occur in the experiments at the smallest volumetric flow rate used in μPIV, i.e., Q = 1 ml/h, for which the relative error in a single realization due to Brownian motion is $\epsilon_{\mathrm{B}} = 0.028$. Since this error is unbiased and we are dealing with steady–state flows, it can be substantially reduced by averaging over groups of particles as suggested by Wereley et al. (2002) and the corresponding uncertainty becomes approximately $\epsilon_{\mathrm{B}}/\sqrt{N}$, where N is the total number of particles in the ensemble average (per each interrogation area). Since each image was divided into interrogation areas of 32 × 32 pixels, which typically each contain a small number of particles per image (around 2–3 particles), and since a minimum of 70 image pairs were used for subsequent ensemble averaging, the final uncertainty due to Brownian motion is less than 0.3%.

3 Numerical

3.1 Governing equations and numerical method

For an incompressible fluid flow, the governing equations for conservation of mass and momentum can be expressed as follows:

$$\nabla \cdot \mathbf{u} = 0, \tag{6}$$

$$\rho\left[\frac{\partial \mathbf{u}}{\partial t} + \nabla \cdot \mathbf{uu}\right] = -\nabla p + \nabla \cdot \boldsymbol{\tau}, \tag{7}$$

where ρ is the density of the fluid, t the time, $\mathbf{u}$ the velocity vector, p the pressure and $\boldsymbol{\tau}$ the total extra stress tensor. In the case of a Newtonian fluid, the total extra stress tensor becomes $\boldsymbol{\tau} = \boldsymbol{\tau}_s = \mu(\nabla\mathbf{u}+\nabla\mathbf{u}^{\mathrm{T}})$. The numerical code used here is applicable to a broad range of viscoelastic models, and, therefore, the constitutive equation, even for the simple case of a Newtonian flow, is solved separately from the momentum equation (Oliveira et al. 1998, 2007; Oliveira and Pinho 1999).

The validity of the continuum hypothesis (implicit in Eqs. 6 and 7) and the no-slip boundary condition were assumed to hold, a result that is well established for Newtonian fluid flows at these micrometer lengthscales (Whitesides and Stroock 2001; Karniadakis et al. 2005).

The agreement between experimental results and the numerical simulations presented here further supports this assumption, at least for Newtonian fluids and the silicone-based material used to fabricate the microgeometries. It also indirectly confirms the dimensional quality of the geometries and of the manufacturing process.

The governing equations above are solved numerically using a finite volume method with a time marching algorithm (Oliveira et al. 1998). In this methodology, the resulting algebraic equations relate the dependent variables (p, $\mathbf{u}$, $\boldsymbol{\tau}$), which are calculated at the center of the cells forming the computational mesh, to the values in the nearby surrounding cells. Non-orthogonal non-uniform block-structured meshes are used to map the computational domain. Central differences are used to discretize the diffusive terms, while the CUBISTA high-resolution scheme (Alves et al. 2003) is employed in the discretization of the advective terms. Because we are interested in steady–state calculations in the present work, the time derivative is discretized with an implicit first-order Euler scheme.

No-slip conditions at the solid walls were imposed as well as symmetry conditions at the two center planes ($x = 0$ and $y = 0$). Therefore, the governing equations were solved for only a quarter of the complete flow domain as explained in the next section (cf. Fig. 2). The outflow boundary condition imposed involves vanishing streamwise gradients ($\partial/\partial x = 0$) of velocity and stress components and a constant gradient of pressure at the downstream channel outlet ($L = L_d$). At the inlet boundary, located well upstream of the region of interest, a uniform velocity profile and null stress components were imposed.

3.2 Computational domain, meshes and dimensionless numbers

Figure 2 provides a zoomed view of a typical mesh used in the computations near the contraction region. The inlet and outlet lengths of the channel were set to be longer ($L_u = L_d = 30w_u$) than in the actual experimental device to ensure that the flow fully develops upstream of the contraction and completely re-develops downstream of the expansion.

The computational meshes had a total number of cells (NC) that varied depending on the Hencky strain used, which is closely related to the definition of contraction ratio, $CR = \exp(\varepsilon_H)$. Another important geometric parameter to be considered is the aspect ratio here defined as AR = h/w. Table 2 shows some of the mesh characteristics, such as the NC and the minimum cell size, of the main four meshes used. These correspond to the experimental geometries described in Sect. 2.1 with channel depth, $h = 46$ µm.

The other relevant dimensionless variable that characterizes the dynamics of the flow through the microgeometry is the Reynolds (Re) number, here defined as:

$$Re = \frac{\rho < V_z >_u w_u/2}{\mu} = \frac{\rho Q}{2h\,\mu}, \tag{8}$$

where Q is the volumetric flow rate and $<V_z>_u$ is the average velocity in the upstream channel ($<V_z>_u = Q/(hw_u)$). For the present conditions and geometries, using water as working fluid, we obtain $Re = 3.21\ Q$, with Q expressed in ml/h.

4 Results

4.1 Flow kinematics

4.1.1 *Measurement validation*

The kinematics of the flow in the planar geometry was quantified using µPIV as described in Sect. 2.2. The first

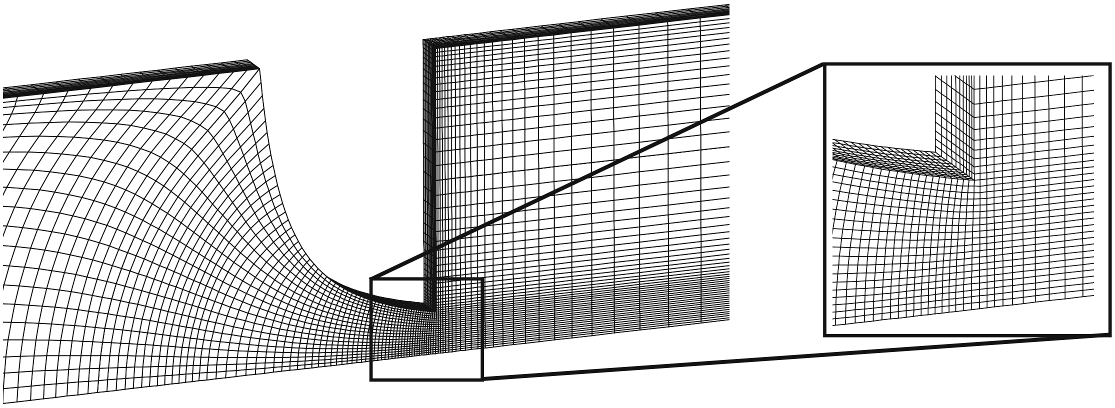

Fig. 2 Zoomed view of the mesh M2 and detail near the expansion plane ($\varepsilon_H = 2.0$). Due to symmetry about the $x = 0$ and $y = 0$ planes only one quarter of the flow geometry shown in Fig. 1 is discretized

Table 2 Main characteristics of the computational meshes

Mesh	Hencky strain	NC	$\Delta x_{\min}/w_c$	$\Delta y_{\min}/w_c$	$\Delta z_{\min}/w_c$
M1	1.0	49920	0.011	0.011	0.010
M2	2.0	50080	0.024	0.022	0.025
M3	3.0	66720	0.026	0.025	0.026
M4	3.7	84160	0.033	0.031	0.032

step toward validating the experimental measurements consisted of comparing the measured axial velocity profiles in fully-developed flow within the large upstream rectangular duct with the corresponding analytical solution for a Newtonian fluid given by White (1991):

$$V_z(x,y) = \frac{12Q}{ab\pi^3}\frac{\sum\limits_{i=1,3,\ldots}^{\infty}\frac{(-1)^{(i-1)/2}}{i^3}\cos(i\pi x/2a)\left(1-\frac{\cosh(i\pi y/2a)}{\cosh(i\pi b/2a)}\right)}{\left(1-\frac{192a}{\pi^5 b}\sum\limits_{i=1,3,\ldots}^{\infty}\frac{\tanh(i\pi b/2a)}{i^5}\right)}, \tag{9}$$

where V_z is the streamwise velocity, a the channel half-width ($w/2$), and b the channel half-depth ($h/2$). For the upstream channel with dimensions $a = w_u/2 = 200$ μm and $b = h/2 = 23$ μm, the dimensionless velocity at the centerline ($x = 0$ and $y = 0$) becomes $V_z/\langle V_z\rangle_u = 48/\pi^3 \times 1.05 = 1.62$.

In Fig. 3, the variation of the streamwise velocity $V_z(x)$ at the center plane ($y = 0$) is plotted. The experimental profile was obtained from a single experiment in the standard way, i.e., using a single set of 70 image pairs centered at the $y = 0$ plane. Because of the low-aspect ratios (AR = h/w_u = 0.12), the velocity profile is flat across 80% of the channel with a constant plateau value $V_z/\langle V_z\rangle_u \approx 1.62$. This figure also contains the profile of streamwise velocity along the y-axis direction, $V_z(y)$, at the $x = 0$ center plane. To construct this profile, each point was obtained by moving the microscope stage in the y-direction and then performing a different ''illumination'' experiment at a different y-plane. For each position along the y-axis direction, the velocity field was measured as described above, and the axial velocity in the plateau region was determined and taken to represent the velocity on the y–z center plane at $x = 0$ for that particular value of y. Close agreement is found between the experimental measurements (symbols) and the analytical solutions (lines) thus validating the experimental procedure. This comparison of the experimental data against the theoretical solution also provides an indirect validation of the dimensional precision and uniformity of the test section.

4.1.2 Contraction region

Experimental and calculated lateral profiles of the streamwise (V_z) and lateral (V_x) velocity components at various axial positions (–400 μm ≤ z ≤ 80 μm), at the center plane ($y = 0$), are compared in Fig. 4 for the geometry with a total Hencky strain of two ($\varepsilon_H = 2.0$) and $Q = 1$ ml/h ($Re = 3.21$). For an axial position far upstream of the contraction plane ($z = -400$ μm), the profiles resemble those of fully-developed flow. As we move toward the contraction plane, the fluid is focused toward the centerline, causing the axial velocity to decrease near the walls, while the lateral velocity increases substantially relative to the fully-developed flow. The maximum streamwise velocity is attained at the centerline ($y = 0$ and $x = 0$) and increases progressively into the contraction. Excellent agreement between the numerical predictions with the experimental data is obtained over the whole flow region and validates the numerical procedure.

In Fig. 5, we show the effect of the flow rate on the measured (symbols) and numerically predicted (thick solid lines) streamwise velocities along the centerline for a fixed Hencky strain ($\varepsilon_H = 2.0$). The profiles evolve from fully developed values in the far upstream part of the channel (where the centerline velocity is constant) to a region where the fluid accelerates as the contraction plane is approached. Within the hyperbolic contraction region, the streamwise velocity increases considerably as the channel narrows due to continuity. As the fluid crosses the expansion plane, it decelerates until the flow re-develops downstream of the

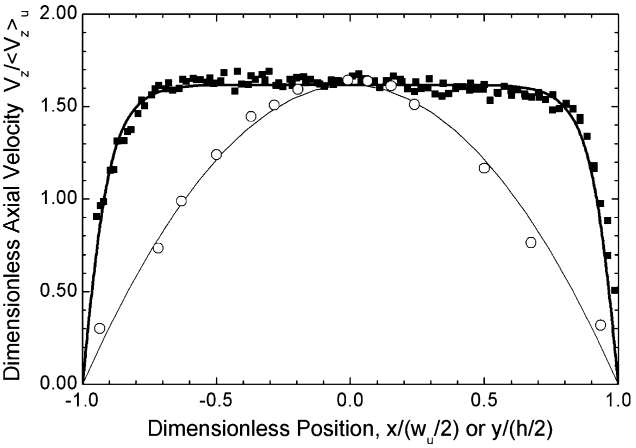

Fig. 3 Comparison of the axial velocity profiles determined experimentally (*symbols*) at constant flow rate $Q = 1$ ml/h ($Re = 3.21$) and the analytical solution (*solid lines*) for Newtonian flow in a rectangular channel (400 × 46 μm^2): (*filled square*) Profile along the x-axis direction (at the center plane $y = 0$); (*open circle*) Profile along the y-axis direction (at the center plane $x = 0$)

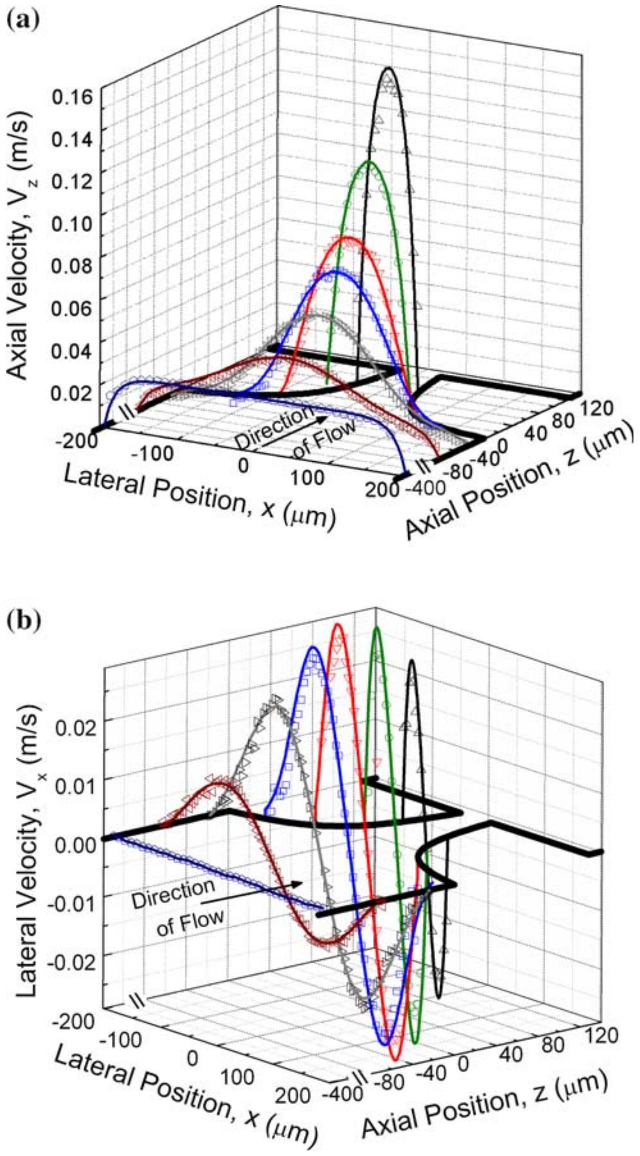

Fig. 4 Comparison of the velocity profiles at the center plane ($y = 0$) determined experimentally (*open symbols*) and numerically (*solid lines*), as a function of the axial and lateral positions for $Q = 1$ ml/h ($Re = 3.21$) and $\varepsilon_H = 2.0$: **a** Velocity component in the z-axis direction; **b** Velocity component in the x-axis direction

contraction. The channel length required for the fluid to regain its fully-developed condition depends linearly on the flow rate (Reynolds number), as in macroscale flows. To make this clear, we present the dimensionless streamwise velocity scaled with the average upstream velocity, $<V_z>_u$, in the inset of Fig. 5, where only the numerical results are displayed, for clarity.

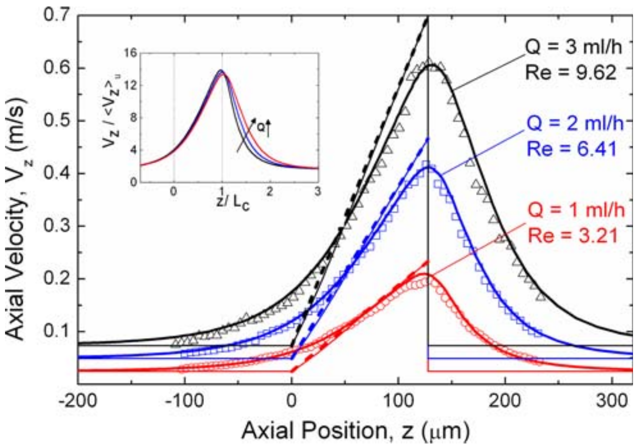

Fig. 5 Effect of flow rate on the axial velocity profile along the centerline ($y = 0$ and $x = 0$) measured experimentally (*open symbols*) and calculated numerically (*thick solid lines*) for a fixed total Hencky strain $\varepsilon_H = 2.0$. The thin lines correspond to the hypothetical fully-developed case (Eq. 10) and the dashed lines to the ideal case with a linear variation in axial velocity between the contraction entrance and exit (Eq. 11). The inset shows the corresponding dimensionless numerical results

In Fig. 5, we also show as thin straight lines the profiles calculated using the quasi-steady approximation for the streamwise velocity along the contraction centerline (i.e., assuming that at each axial location the flow fully develops instantaneously), which is related to the average velocity by (White 1991):

$$V_{z,\,\text{centerline}} = k < V_z >, \tag{10}$$

where k is only a function of the channel aspect ratio and is obtained from the exact fully-developed solution in a rectangular channel (Eq. 9). The difference between this analytical result and the actual numerical (and experimental) data is principally a consequence of not considering contraction entrance and expansion exit effects.

The corresponding strain rates along the centerline of the hyperbolic contraction can be computed from the axial velocity profiles for each set of flow conditions and are plotted in Fig. 6. For the sake of comparison, we have also plotted, as dashed lines in Figs. 5 and 6, the profiles corresponding to the ideal case of a linear velocity variation between the entrance and exit of the contraction. In the ideal case, the strain rate at the centerline is constant and can be calculated as:

$$\dot{\varepsilon}_{\text{centerline}} = \left(k_c \frac{Q}{h\,w_c} - k_u \frac{Q}{h\,w_u} \right) \Big/ L_c, \tag{11}$$

where k_u and k_c are determined from Eqs. 9 and 10. For the geometry with $\varepsilon_H = 2.0$, the parameters k_u and k_c are ~1.62 and 2.09 at the contraction entrance (AR = h/w_u = 0.12) and exit (AR = h/w_c = 0.85), respectively.

As seen in Fig. 6 the strain rate is not constant along the contraction. In addition to entrance and exit effects, which spread through most of the contraction length, there are

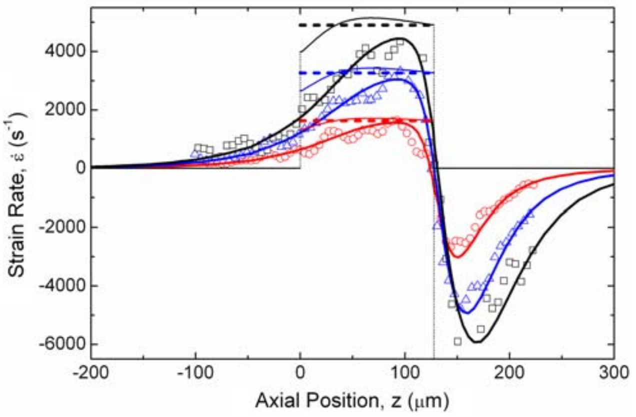

Fig. 6 Effect of flow rate on the strain rate profiles along the centerline for $\varepsilon_H = 2.0$: $Q = 1$ ml/h, $Re = 3.21$ (*open circle*); $Q = 2$ ml/h, $Re = 6.41$ (*open triangle*); and $Q = 3$ ml/h, $Re = 9.62$ (*open square*). The *symbols* correspond to experimental data, the *thick lines* to data from numerical predictions, the *thin lines* to the hypothetical fully-developed case (Eq. 10) and the *dashed lines* to the ideal case with a linear variation between the contraction entrance and exit (Eq. 11)

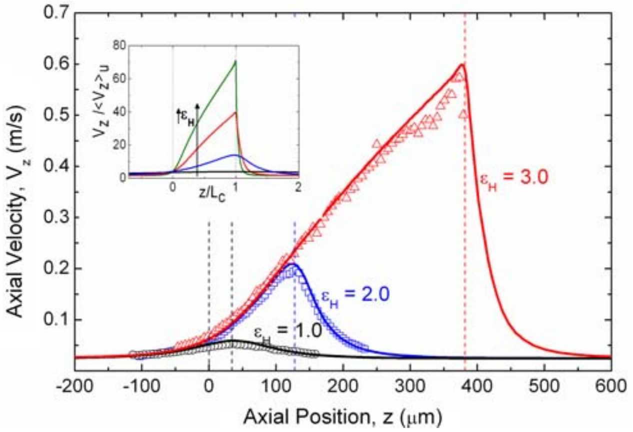

Fig. 7 Effect of the total Hencky strain on the axial velocity profile along the *centerline* ($y = 0$ and $x = 0$) measured experimentally (*open symbols*) and calculated numerically (*thick solid lines*) for a fixed flow rate $Q = 1$ ml/h ($Re = 3.21$). The inset shows numerical results at Hencky strains of 1.0, 2.0, 3.0 and 3.7. The *dashed vertical lines* indicate the beginning and end of the contraction sections for each strain

two other effects that need be taken into consideration. First, the aspect ratio (AR = h/w) is not constant along the contraction and, therefore, the strain rate also varies, even for the hypothetical quasi-steady case (thin solid lines). Second, the flow Reynolds numbers are not sufficiently high to limit viscous effects to a narrow boundary layer and wall effects are therefore not negligible.

Figure 7 illustrates the effect of the total Hencky strain on the axial velocity profile along the centerline at a fixed Reynolds number ($Re = 3.21$). As the Hencky strain increases, the change in velocity through the converging section becomes much larger and varies almost linearly with axial position. For converging geometries with higher Hencky strains, it is expected that there will be a region of the contraction, which is not affected by entrance and/or exit effects. However, the strain rate is only truly constant when either the Reynolds number is high or when the depth of the channel is substantially smaller than the channel width (AR << 1) leading to a Hele–Shaw flow. This asymptotic behavior is demonstrated in Fig. 8 for two different geometries with $\varepsilon_H = 2.0$ and 3.0. It is interesting to note that entrance effects are approximately the same independently of the geometry (Hencky strain) used, particularly when h is small (i.e., when a Hele–Shaw flow is approached). As the depth of the channel is reduced, the flow away from the lateral walls of the z–x planes becomes essentially controlled by the spanwise gradients of viscous forces and the pressure field $\left(\mu\partial^2 V_z/\partial y^2 = (\partial p/\partial z);\ \mu\partial^2 V_x/\partial y^2 = (\partial p/\partial x)\right)$, from which the irrotational flow condition $(\partial V_z/\partial x - \partial V_x/\partial z = 0)$ is recovered as for potential flow (Acheson 1990). Therefore, streaklines become independent of y (even though the velocity components exhibit a strong dependence) and coincident with those observed for a potential fluid away from the lateral walls. Although reducing h may seem like an appropriate way to achieve a homogeneous extensional flow, it leads to increasingly strong shear effects due to the increase in τ_{zy} (and in pressure drop) and the dimensionless entry pressure drop due to extensional effects decreases substantially (M. S. N Oliveira et al. 2007, submitted data). This makes it unfeasible to extract an apparent extensional viscosity simply from pressure drop measurements.

It is clear from the experimental results in Fig. 7 that at higher Hencky strains the velocity profiles become harder to measure very close to the expansion plane, because of

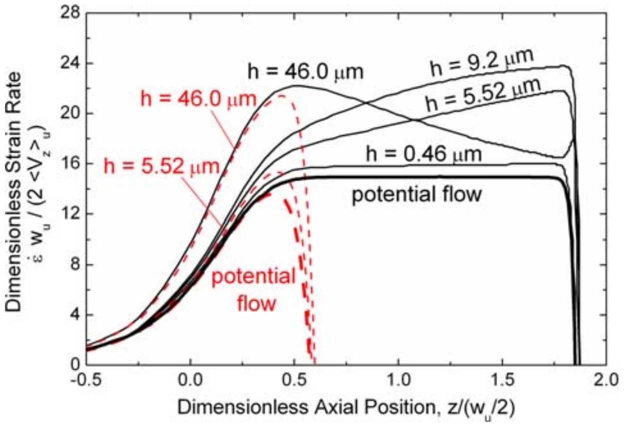

Fig. 8 Dimensionless strain rate profiles along the centerline under creeping flow conditions for $\varepsilon_H = 2.0$ (*dashed lines*) and $\varepsilon_H = 3.0$ (*solid lines*) for various channel depths

the proximity of the walls, the larger velocity gradients and the high contraction ratios. Nevertheless, in this region, the experimental measurements are in good agreement with the numerical solutions for all cases studied. This can be assessed in more detail from the contour plots of the axial velocity at the center plane ($y = 0$) that are presented in Fig. 9. Although the experimental contour plots are naturally not as smooth as the corresponding numerical plots, the μPIV and computed velocity fields are in good quantitative agreement.

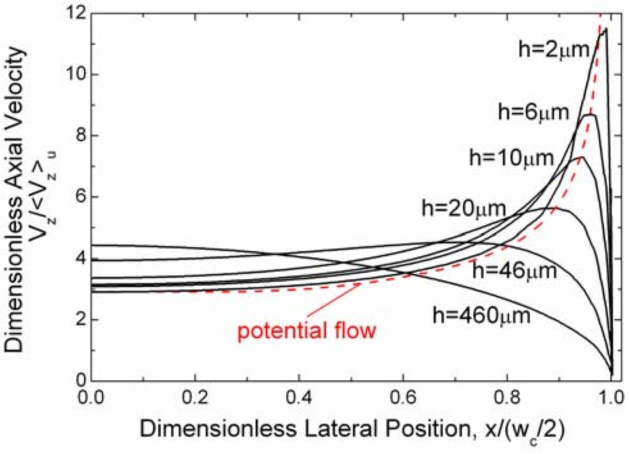

Fig. 10 Axial velocity profiles predicted numerically under creeping flow conditions at the intersection between the center plane ($y = 0$) and the expansion plane ($z = 34.4$ μm) for $\varepsilon_H = 1.0$ and a range of microfluidic channel depths $2 \leq h \leq 460$ μm

In Fig. 9, we also compare the velocity fields at different Hencky strains for the same flow rate. It is interesting to note that whereas the maximum axial velocity for $\varepsilon_H = 2.0$ is located at the centerline, as observed previously in Fig. 4, in the smaller Hencky strain case two off-center velocity maxima are observed, both experimentally and numerically. As already discussed, 3D effects can play an important role in this flow and, similarly, the development of off-center maxima was seen to be closely related to the geometry depth and therefore to the aspect ratio. Figure 10 shows the effect of varying the channel depth h on the computed axial velocity profile along the lateral direction at the expansion plane. These results were obtained for creeping flow conditions ($Re \to 0$) at the center plane with a contraction of $\varepsilon_H = 1.0$. As anticipated from Fig. 9, for the depth used in the experiments, $h = 46$ μm, the maximum velocity is already located off-center. The peak corresponding to the maximum velocity is seen to become more pronounced and moves toward the corner of the reentrant expansion as the channel depth decreases. This shift arises because the ratio between the diffusion time in the x-direction and the transit time through the contraction becomes progressively smaller with h; the perturbation imposed by the contraction on the z–x planes does not have the time to fully diffuse toward the center plane. At the smaller depths, the diffusive fluxes of momentum in the y-direction ‘‘dominate’’ compared to those in other

Fig. 9 Axial velocity contour plots $V_z(x, z)$ at the center plane ($y = 0$) at $Q = 1$ ml/h ($Re = 3.21$). Comparison between experimental measurements (*left*) and numerical predictions (*right*) for: **a** $\varepsilon_H = 2.0$; **b** $\varepsilon_H = 1.0$

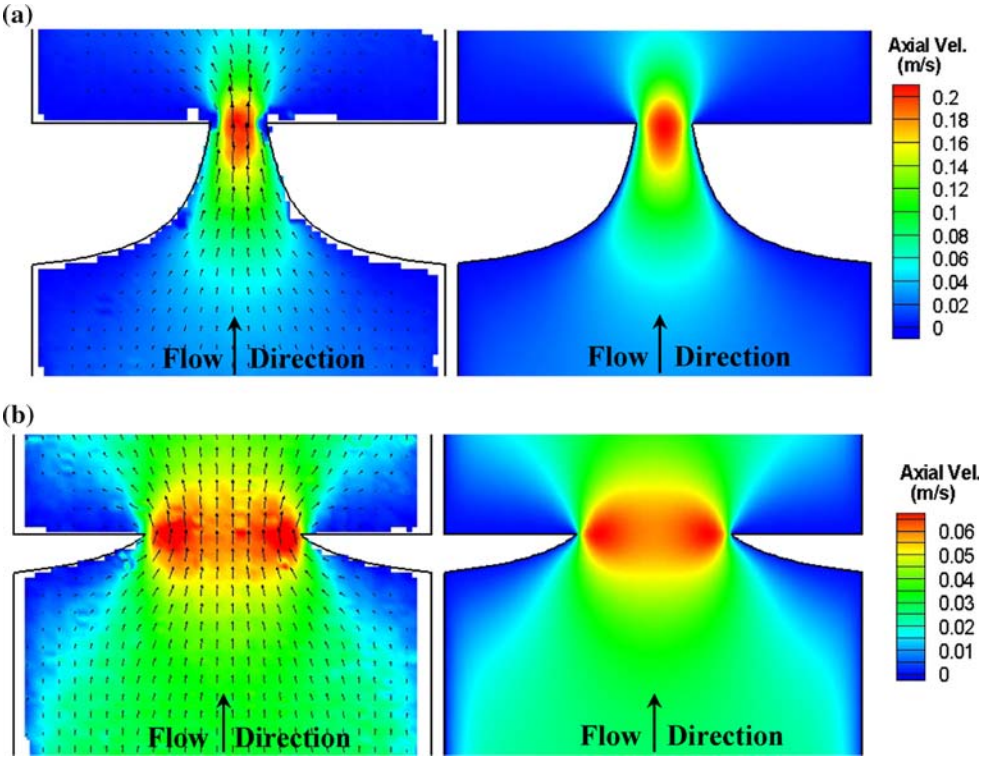

directions and geometry changes in x–z planes act slowly (i.e., $\Delta t_x >> \Delta t_y$ with $\Delta t_\ell \approx \ell^2/v$ and $\ell = x, y$ with $x > y$). The flow at constant y-planes approaches a 2D potential flow, as illustrated in Fig. 10 for the $y = 0$ center plane.

These competing effects of momentum diffusion in the x- and y-directions are also seen clearly in the contour plots of the axial velocity in Fig. 11a for $\varepsilon_H = 1.0$ and Fig. 11b for the longer contraction with $\varepsilon_H = 3.0$. In Fig. 11a, the flow in the actual experimental configuration (h = 46 μm) is compared with that for devices with smaller (h = 4.6 μm) and larger (h = 460 μm) depths. Increasing the depth of the channel causes the diffusion in the x–z plane to dominate over the diffusion in the y-axis direction and the flow in the center plane approaches a 2D Stokes' flow (e.g., h = 460 μm). In this case, there is only one maximum located at the centerline ($x = 0$). With the longer hyperbolic contraction of Fig. 11b, the maximum axial velocity once again approaches the expansion corners with decreasing h (e.g., h = 0.46 μm), as expected for a Hele–Shaw flow. However, the conditions required to generate the off-center maxima now require a smaller value of h because the narrower physical dimensions of the contraction exit decrease the diffusion time on the x–z plane. Hence, this phenomenon is indirectly controlled by the ratio AR = h/w.

4.1.3 Expansion region

A sequence of computed streaklines are shown in Fig. 12 for $\varepsilon_H = 2.0$ and increasing flow rates in the contraction and expansion regions. As we move closer to the contraction plane, the fluid is forced toward the centerline and the

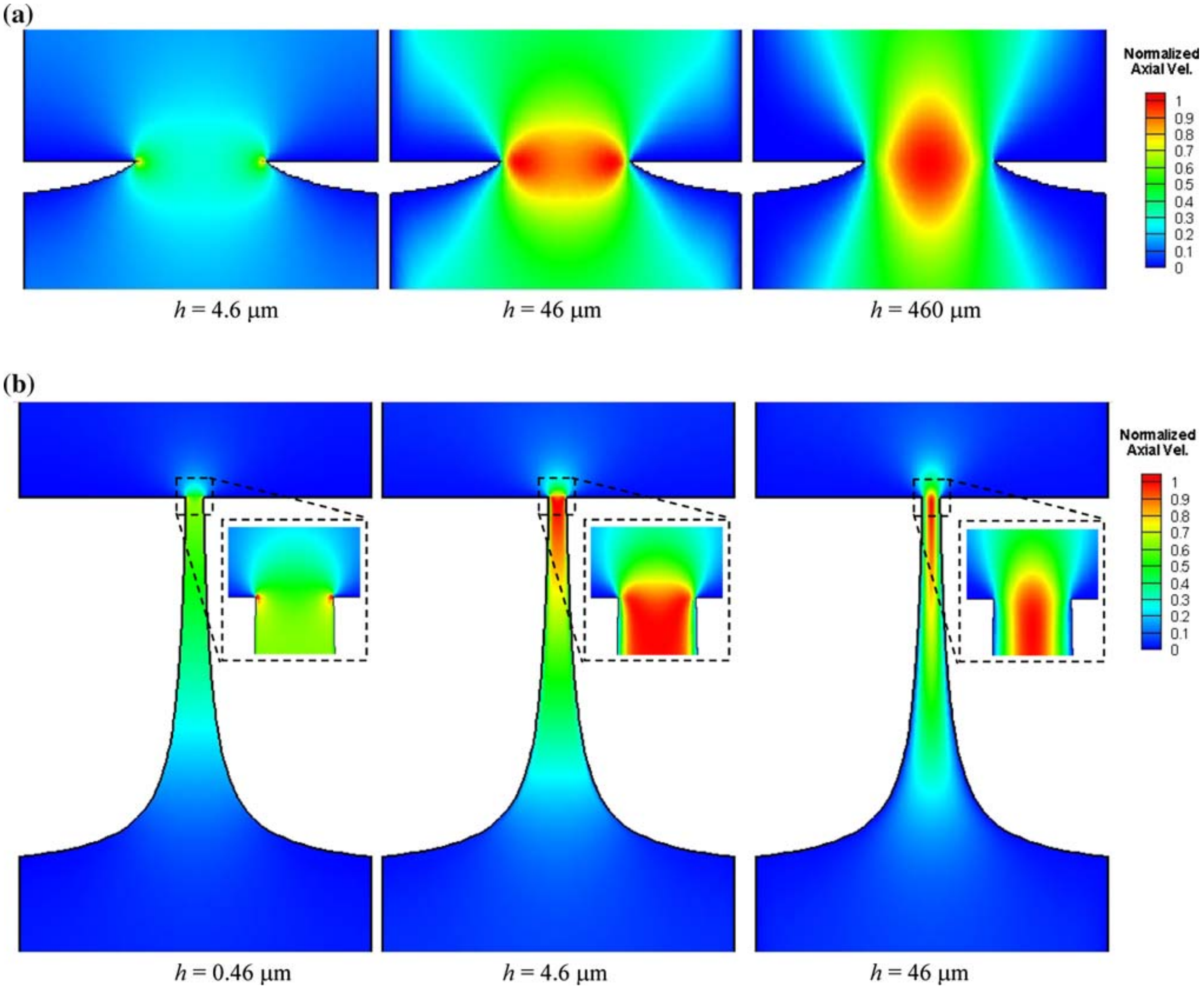

Fig. 11 Numerical contour plots of the normalized axial velocity ($V_z/V_{z,\max}$) at the center plane ($y = 0$) obtained under creeping flow conditions for **a** $\varepsilon_H = 1.0$ and **b** $\varepsilon_H = 3.0$

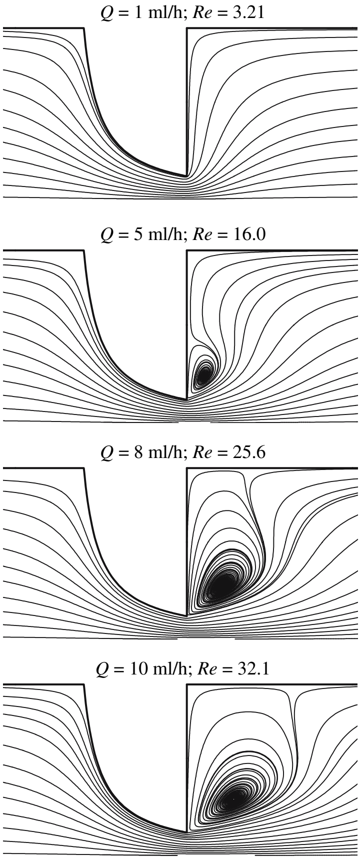

Q = 1 ml/h; Re = 3.21

Q = 5 ml/h; Re = 16.0

Q = 8 ml/h; Re = 25.6

Q = 10 ml/h; Re = 32.1

Fig. 12 Numerically predicted streaklines at the center plane ($y = 0$) for $\varepsilon_H = 2.0$ and increasing flow rates

streakline patterns are qualitatively similar for all the flow rates. However, the streaklines corresponding to the higher flow rates are pushed toward the contraction wall due to the higher streamwise velocities (and the increased importance of fluid inertia). At low flow rates, fluid elements downstream of the expansion plane begin to reattach to the wall as soon as they exit the contraction; by contrast, inertial effects result in the development and enhancement of a lip vortex as we increase the Reynolds number (e.g., $Re = 16.0$). The recirculation grows with the fluid inertia and at $Re = 25.6$ it already extends to the side-wall close to the salient corner ($x/w_u \approx 0.5$). The vortices continue to expand downstream for the entire range of flow rates tested (up to $Re = 32.1$). Eventually, a flow asymmetry develops at higher flow rates, as commonly observed in 2D-planar expansion flows (Wille and Fernholz 1965; Chiang et al. 2000; Oliveira 2003) and the flow becomes unsteady at even higher flow rates. These regimes are outside the range of conditions useful for rheometric purposes and therefore are not studied in this work.

The size of this recirculation depends not only on the Reynolds number, but also on the expansion ratio as shown in the predicted streaklines of Fig. 13 for a fixed flow rate and four different Hencky strains. The Reynolds number is $Re = 9.62$, so that inertial effects are not negligible. At low-Hencky strains, the behavior is akin to that of creeping flow in the sense that there is no flow separation, but as the gap at the end of the contraction narrows and the exit jet strengthens, a lip vortex forms and expands. These results indicate that as the Hencky strain is increased, the critical Reynolds number beyond which no further rheometrical tests are to be carried out should be reduced. Overall, the vortex enhancement mechanism is similar to that observed in studies of planar geometries with abrupt contraction-expansions (Townsend and Walters 1994; Rodd et al. 2005).

4.2 Viscous pressure drop across the contraction

The variation with Reynolds number ($1.28 < Re < 32.1$) of the measured global pressure drop across the hyperbolic contraction is plotted in Fig. 14 for geometries with total Hencky strains of $\varepsilon_H = 1.0$, 2.0, and 3.0. The pressure taps were located 3×10^{-3} m upstream and downstream of the contraction plane and we also show in the figure the corresponding numerical computations. The pressure drop increases almost linearly with the flow rate as anticipated from a viscous flow scaling, and close agreement is observed between the numerical and experimental results. The corresponding range of characteristic elongation rates is $6.0 \times 10^2\ \mathrm{s}^{-1} < \dot{\varepsilon} < 1.6 \times 10^4\ \mathrm{s}^{-1}$. For comparison, we also indicate by solid lines the hypothetical pressure drop determined assuming the flow fully develops instantaneously at each axial position. According to the lubrication analysis of Lauga et al. (2004), this estimate is expected to be accurate whenever the channel cross-section varies smoothly along the axial position, but in our microgeometries there are sudden changes of the cross-section at the entrance and exit of the hyperbolic section; therefore, it is not surprising that this estimate is consistently lower than the corresponding measured values.

5 Conclusions

We have presented a detailed study of the flow of a Newtonian fluid through 3D-planar microgeometries containing a hyperbolic contraction followed by an abrupt expansion, aimed at assessing its potential application as an extensional microrheometer. The work was carried out from both an experimental and a numerical perspective and the corresponding results are in extremely good agreement with each other. Although at first sight the flow may appear quasi-two dimensional in nature, we have demonstrated

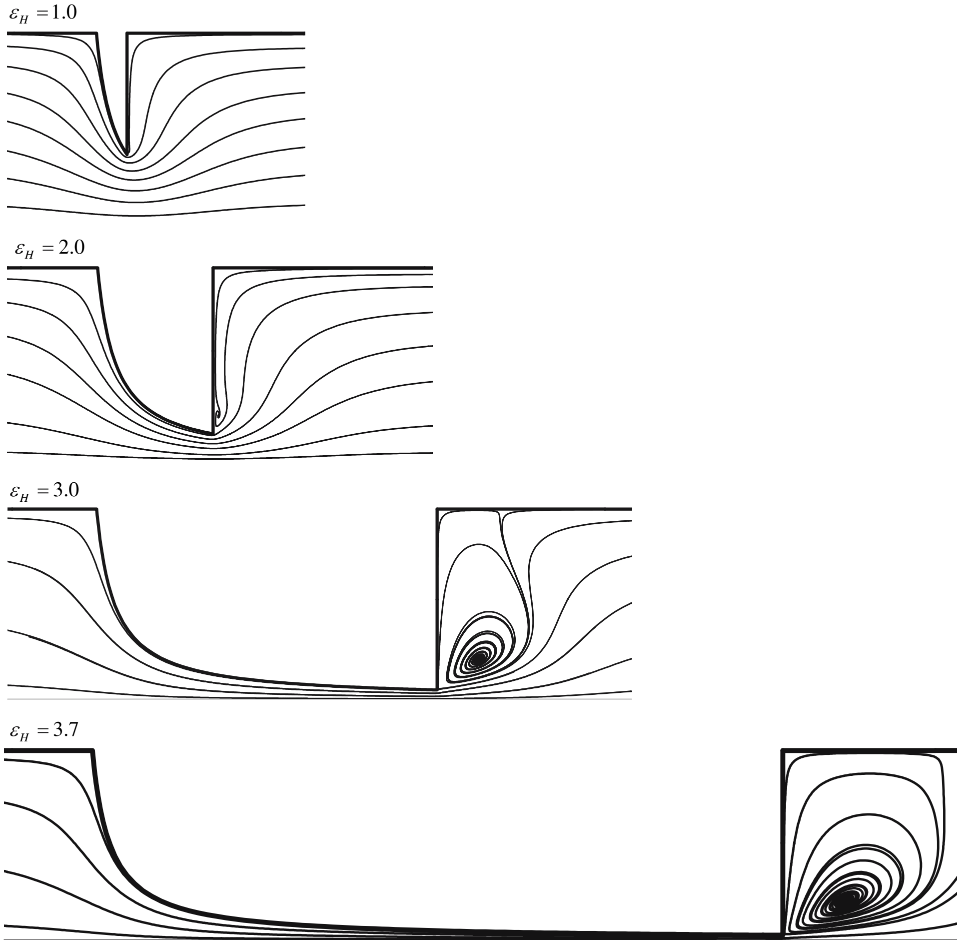

Fig. 13 Numerically predicted streaklines at the center plane ($y = 0$) for $Re = 9.62$ ($Q = 3$ ml/h) and four different Hencky strains

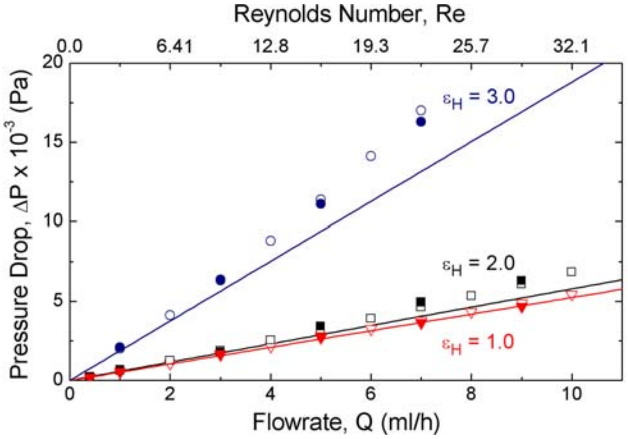

Fig. 14 Effect of inertia on the total pressure drop determined experimentally (*filled symbols*) and numerically (*open symbols*) for ε_H = 1.0, 2.0 and 3.0. The *solid lines* correspond to hypothetical pressure drops if there were no entrance or exit effects and assuming the flow is fully-developed everywhere

that there are important 3D effects, which depend on the aspect ratio and a simple 2D approach is often qualitatively inadequate to describe the flow patterns. For geometries with very low-aspect ratios, a Hele–Shaw flow approximation is appropriate and, therefore, the flow patterns resemble those of 2D-potential flow and not planar 2D viscous flow, as often assumed erroneously in numerical works in microfluidic devices.

The μPIV technique allowed accurate measurements of the velocity field in the contraction region for a range of flow rates (1 ml/h $\le Q \le$ 3 ml/h) and Hencky strains ($1.0 \le \varepsilon_H \le 3.0$). In the upstream channel away from the contraction, the axial velocity profiles are steady and fully developed, but as the fluid approaches the contraction, it accelerates and the maximum centerline velocity increases. As the Reynolds number is increased, the effects of the expansion are felt further downstream and lip vortices are seen to develop and grow downstream of the contraction. The development of a single-centered velocity maximum or double off-center velocity maxima at the contraction throat have also been measured, predicted numerically and explained physically. Experimental measurements of the pressure drop were also performed and could be extended to a wider range of flow conditions than those attainable using μPIV. The pressure drop across the contraction was found to vary approximately linearly with the Reynolds number or flow rate. However, contrary to our expectations, the strain rate along the centerline of the converging geometry with $\varepsilon_H = 2.0$ was not constant. For this geometry, the length of the contraction is not sufficient to guarantee the existence of a locally fully-developed region without important entrance and exit effects. Furthermore, the wall effects are not negligible and the effective aspect ratio of the flow varies along the contraction. For the higher strains, these effects are not as severe and there is a region of approximately linear velocity increase along the channel as the geometry depth is reduced. However, in this limit, the viscous shearing contribution to the total pressure variation dominates and makes it difficult to extract purely extensional effects. This problem will be reduced in severity when the fluids are viscoelastic in nature, because they will develop a strong additional elastic stress as a result of the elongational flow. However, the complex interplay of shearing and extensional flows is still far from resolved, and substantial computational efforts must be made to optimize the shape of the converging geometry, particularly if such devices are to be used as microfluidic extensional rheometers. The quantitative agreement between simulations and experiments—both for pointwise kinematic measurements and for global measures, such as the pressure drop-flow rate relationship—suggests that computational fluid dynamics can play an important role in guiding the design of microfluidic rheometers.

Acknowledgments M. S. N. Oliveira would like to thank Fundação para a Ciência e a Tecnologia (FCT), Portugal for the financial support (SFRH/BPD/15005/2004). M. S. N. Oliveira, M. A. Alves and F. T. Pinho acknowledge the financial support provided under program POCI2010 by FCT and FEDER: project POCI/EME/59338/2004 (M. S. N. Oliveira, M. A. Alves, and F. T. Pinho) and project POCI/EQU/59256/2004 (M. A. Alves). The experimental portion of this work was carried out in the Hatsopoulos Microfluids Laboratory at MIT using equipment provided by the National Science Foundation under grant CTS-0116486.

References

Acheson DJ (1990) Elementary fluid dynamics. Clarendon Press, Oxford

Alves MA, Oliveira PJ, Pinho FT (2003) A convergent and universally bounded interpolation scheme for the treatment of advection. Int J Numer Meth Fl 41:47–75

Barnes HA, Hutton JF, Walters K (1989) An introduction to rheology. Elsevier, Amsterdam

Brown RA, McKinley GH (1994) Report on the VIIIth international workshop on numerical methods in viscoelastic flows. J Non-Newton Fluid Mech 52:407–413

Chiang TP, Sheu TWH, Wang SK (2000) Side wall effects on the structure of laminar flow over a plane-symmetric sudden expansion. Comput Fluids 29:467–492

Cogswell FN (1978) Converging flow and stretching flow: a compilation. J Non-Newton Fluid Mech 4:23–38

Einstein A (1905) On the movement of small particles suspended in a stationary liquid demanded by the molecular-kinetic theory of heat. In: Theory of Brownian Movement. Dover Publications Inc., New York, pp 1–18

Everage AE Jr, Ballman RL (1978) The extensional flow capillary as a new method for extensional viscosity measurement. Nature 273:213–215

Feigl K, Tanner FX, Edwards BJ, Collier JR (2003) A numerical study of the measurement of elongational viscosity of polymeric fluids in semi-hyperbolically converging die. J Non-Newton Fluid Mech 115:191–215

Groisman A, Quake SR (2004) A microfluidic rectifier: anisotropic flow resistance at low Reynolds numbers. Phys Rev Lett 92:1–4

Hassager O (1988) Working group on numerical techniques (Vth workshop on numerical methods in non-Newtonian flow). J Non-Newton Fluid Mech 29:2–5

Hermansky CG, Boger DV (1995) Opposing-jet viscometry of fluids with viscosity approaching that of water. J Non-Newton Fluid Mech 56:1–14

James DF (1991) Flow in a converging channel at moderate Reynolds number. AIChE J 37:59–64

James DF, Chandler GM, Armour SJ (1990) A converging channel rheometer for the measurement of extensional viscosity. J Non-Newton Fluid Mech 35:421–443

Karniadakis G, Beskok A, Aluru NR (2005) Microflows and nanoflows: fundamentals and simulation. Springer Verlag, New York, NY

Kang K, Koelling KW, Lee LJ (2006) Microdevice end pressure evaluations with Bagley correction. Microfluid Nanofluid 2:223–235

Kang K, Lee LJ, Koelling KW (2005) High shear microfluidics and its application in rheological measurement. Exp Fluids 38:222–232

Lauga E, Stroock AD, Stone HA (2004) Three-dimensional flows in slowly varying planar geometries. Phys Fluid 16:3051–3062

McDonald JC, Duffy DC, Anderson JR, Chiu DT, Wu HK, Schueller OJA, Whitesides GM (2000) Fabrication of microfluidic systems in poly(dimethylsiloxane). Electrophoresis 21:27–40

Meinhart CD, Wereley ST, Gray MHB (2000) Volume illumination for two-dimensional particle image velocimetry. Meas Sci Technol 11:809–814

Ng JMK, Gitlin I, Stroock AD, Whitesides GM (2002) Components for integrated poly(dimethylsiloxane) microfluidic systems. Electrophoresis 23:3461–3473

Oliveira PJ (2003) Asymmetric flows of viscoelastic fluids in symmetric planar expansion geometries. J Non-Newton Fluid Mech 114:33–63

Oliveira PJ, Pinho FT (1999) Numerical procedure for the computation of fluid flow with arbitrary stress-strain relationships. Numer Heat Tr B-Fund 35:295–315

Oliveira PJ, Pinho FT, Pinto GA (1998) Numerical simulation of non-linear elastic flows with a general collocated finite-volume method. J Non-Newton Fluid Mech 79:1–43

Olsen MG, Adrian RJ (2000) Out-of-focus effects on particle image visibility and correlation in microscopic particle image velocimetry. Exp Fluids 29:S166–S174

Prasad AK, Adrian RJ, Landreth CC, Offutt PW (1992) Effect of resolution on the speed and accuracy of particle image velocimetry interrogation. Exp Fluids 13:105–116

Rodd LE (2006) Planar entry flow of low viscosity elastic fluids in micro-fabricated contraction geometries. Ph.D. Thesis, Department of Chemical and Biomolecular Engineering, University of Melbourne, Melbourne, VIC, Australia

Rodd LE, Scott TP, Boger DV, Cooper-White JJ, McKinley GH (2005) The inertio-elastic planar entry flow of low-viscosity elastic fluids in micro-fabricated geometries. J Non-Newton Fluid Mech 129:1–22

Rodd LE, Cooper-White JJ, Boger DV, McKinley GH (2007) Role of the elasticity number in the entry flow of dilute polymer solutions in micro-fabricated contraction geometries. J Non-Newton Fluid Mech (in press)

Santiago JG, Wereley ST, Meinhart CD, Beebe DJ, Adrian RJ (1998) Particle image velocimetry systems for microfludics. Exp Fluids 25:316–319

Scott TP (2004) Contraction/expansion flow of dilute elastic solutions in microchannels. M.S. Thesis, Mechanical Engineering Department, MIT, Cambridge, MA, USA

Sharp KV, Adrian RJ (2004) Transition from laminar to turbulent flow in liquid filled microtubes. Exp Fluids 36:741–747

Shaw MT (1975) Flow of polymer melts through a well-lubricated, conical die. J Appl Polym Sci 19:2811–2816

Squires TM, Quake SR (2005) Microfluidics: fluid physics at the nanoliter scale. Rev Mod Phys 77:977–1026

Stone HA, Stroock AD, Ajdari A (2004) Engineering flows in small devices: microfluidics toward a Lab-on-a-Chip. Annu Review Fluid Mech 36:381–411

Tsai C-H, Chen H-T, Wang Y-N, Lin C-H, Fu L-M (2006) Capabilities and limitations of 2-dimensional and 3-dimensional numerical methods in modeling the fluid flow in sudden expansion microchannels. Microfluid and Nanofluid. doi:10.1007/s10404-006-0099-2

Townsend P, Walters K (1994) Expansion flows of non-Newtonian liquids. Chem Eng Sci 49:749–763

Wereley ST, Meinhart CD (2004) Micron-resolution particle image velocimetry. In: Breuer KS (ed) Microscale diagnostic techniques. Springer, Berlin

Wereley ST, Gui L, Meinhart CD (2002) Advanced algorithms for microscale particle image velocimetry. AIAA J 40:1047–1055

White FM (1991) Viscous fluid flow. McGraw-Hill, New York

Whitesides GM, Stroock AD (2001) Flexible methods for microfluidics. Phys Today 54:42–48

Wille R, Fernholz H (1965) Report on first European mechanics colloquium on coanda effect. J Fluid Mech 23:801–819